Nonlinear Dyn
https://doi.org/10.1007/s11071-022-07494-4

ORIGINAL PAPER

Theoretical modeling and experimental evaluation of a magnetostrictive actuator with radial-nested stacked configuration

Long Chen · Yuchuan Zhu · Jie Ling · Zhao Feng

Received: 30 September 2021 / Accepted: 27 April 2022

Abstract Stacked magnetostrictive actuator (SMA) has the advantages of high energy density and high bandwidth, but the output stroke is relatively small and accompanied by strong hysteresis nonlinearity. Introducing the radial-nested stacked configuration, the stroke of a SMA can be increased without deteriorating its bandwidth. However, this configuration consists of three magnetostrictive rods of different shapes which brings more serious asymmetric hysteresis nonlinearity and poses a great challenge on the theoretical modeling of the actuator. In this paper, a magnetic equivalent circuit (MEC) model is established to describe the magnetic characteristic of radial-nested stack. Then, a nonlinear dynamic magnetization model is proposed with the combination of the MEC model and the Jiles-Atherton model. Finally, by considering the multi-degree-of-freedom (MDOF) mechanical dynamic system, a multiphysics comprehensive dynamic (MCD) model is established. What's more, a prototype of radial-nested stacked Terfenol-D actuator (RSTA) is fabricated, a series of simulations and experiments are conducted to evaluate the proposed models. The parameters that cannot be calculated or measured in the model are identified by employing the multi-island genetic algorithm. Results show that: (a) the MEC model can accurately calculate the magnetic distribution of the RSTA with an error less than 0.2% compared with a finite element model; (b) the MCD model can accurately describe the RSTA output hysteresis nonlinearity under different operating frequencies and amplitudes with a root-mean-square (RMS) error less than 1.1 μm (1.76%).

Keywords Magnetostrictive actuator · Radial-nested stack · Asymmetric hysteresis nonlinearity · Multi-degree-of-freedom dynamic system · Theoretical modeling

1 Introduction

Stacked magnetostrictive actuator (SMA) provides displacement under the excitation of external magnetic field [1]. This noncontact-type driving pattern brings extremely high reliability compared with those smart material actuators with contact-type driving patterns. Thanks to the advantages of high bandwidth and high energy density, magnetostrictive actuator [2,3], as a novel electro-mechanical converter, has been applied in many industrial engineering fields [4–7], especially in the aeronautical actuation systems with the requirements of quick response and precision motion [8].

L. Chen · Y. Zhu (✉)· J. Ling (✉)
The National Key Laboratory of Science and Technology on Helicopter Transmission, Nanjing University of Aeronautics and Astronautics, Nanjing 210016, Jiangsu, China
e-mail: meeyczhu@nuaa.edu.cn

J. Ling
e-mail: meejling@nuaa.edu.cn

Z. Feng
Faculty of Science and Technology, University of Macau, Taipa 999078, Macau, China

Published online: 13 May 2022

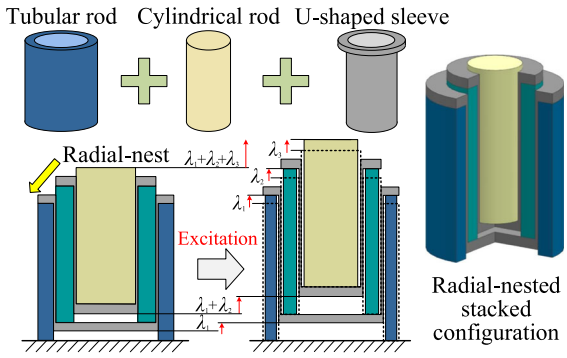

Fig. 1 The radial-nested stacked configuration

However, the major stumbling block for SMA further applications is that the output stroke of SMA is relatively small and accompanied by strong dynamic hysteresis nonlinearity [9–11]. The output displacement of the SMA is proportional to its length. But traditional SMAs are restricted by their small magnetostrictive strain rate which is normally less than 0.2%. Therefore, traditional SMAs are not able to provide enough output stroke in a restricted volume. Although the adoption of amplification mechanism can effectively increase the stroke in a relatively small volume [12,13], the bandwidth of the actuator will seriously decrease at the expense. To tackle this problem, a two-dimensional stacked magnetostrictive actuator (TSMA) with high bandwidth and large stroke was proposed in our previous work in [14]. Different from traditional displacement amplification mechanisms based on lever [15], hydraulic [16] and buckling [17] principles, the TSMA realizes direct displacement amplification through the novel structure of radial-nested stacked configuration, as shown in Fig. 1. In the configuration, U-shaped sleeves were employed to support the radial-nested stacking of three magnetostrictive rods. The stroke of TSMA can reach 65 μm, the displacement amplification ratio is achieved as 2.8 which means that the length of TSMA is only 1/3 of traditional SMAs, and the working bandwidth is kept as 500 Hz.

Unfortunately, this special radial-nested stacked configuration also brings nonuniform magnetic distribution, strong asymmetric hysteresis nonlinearity and complex mechanical dynamic system. The radial-nested magnetostrictive stack contains three magnetostrictive rods of different shapes and sizes, which are stretched at the same time during operation, and the displacement is transmitted through the U-shaped sleeves. On the one hand, the internal magnetic distribution of the actuator with radial-nested stacked configuration becomes nonuniform and the output characteristics become more difficult to predict. On the other hand, this makes the nonlinear dynamic magnetization process and mechanical dynamic characteristics extremely complicated compared with traditional actuators.

As a result, it is of a great challenge to build the theoretical model of the magnetostrictive actuator with such class of structure, i.e., the radial-nested stacked configuration to analyze the output performances and design the controller of the actuator, which is essential for the SMA further applications [18–21].

In terms of magnetic modeling, the magnetic equivalent circuit (MEC) modeling method which equates various parts in the magnetic flux path to the resistance in the circuit, and the magnetic flux is equivalent to current and solved by Kirchhoff's law, has proved to be an effective method [22–25]. In the study of magnetostrictive actuators [26,27], MEC model has been used to analyze the magnetic circuit structure and serve as a guide for the optimal design. However, the magnetostrictive actuator in existing studies is driven by a single cylindrical magnetostrictive rod, and its magnetic circuit presents a series structure. The parallel magnetic circuit analysis and modeling work for the radial-nested stacked magnetostrictive actuator has not been carried out yet.

With respect to the dynamic modeling of magnetostrictive actuator, it can be divided into three parts: electric input dynamic, nonlinear magnetization dynamic and mechanical dynamic. First, the electrical input model has been established in our previous work [28]. Second, the existing nonlinear magnetization modeling methods mainly include phenomenological modeling and physics-based modeling, in which the physics-based Jiles-Atherton (J-A) model [29] is the most widely used. Niu et al. [30] proposed a hybrid model of a magnetostrictive actuation system with the employment of J-A model. To describe the dynamic magnetization process of the magnetostrictive electro-hydraulic actuator, the J-A model was adopted by Zhu et al. [31]. Liu et al. [32] proposed a dynamic J-A model in order to improve controllability and stability of a magnetostrictive actuator. Third, in mechanical dynamic modeling, vibration model is commonly used to describe the dynamic characteristics of mechanical parts of actuation systems [33,34]. Gu et al. [35] modeled a magnetostrictive actuator as a mass-spring-

damper system in a frequency band within the first mechanical mode of vibration. Li et al. [36] also used the vibration model to simplify the mechanical dynamics response of the magnetostrictive actuator to a mass-spring-damping system.

However, the magnetostrictive actuators in existing studies only contain a single magnetostrictive rod, and the established model cannot describe the nonuniform magnetic distribution and the eddy current effect of radial-nested stack which contains three different shapes rods. Therefore, the nonlinear dynamic magnetization process of the radial nested magnetostrictive stack cannot be calculated accurately. Similarly, their mechanical dynamic systems are all single-degree-of-freedom (SDOF) dynamic systems. The MDOF dynamic system brought by the radial-nested stacked configuration has not been analyzed effectively.

In this paper, to accurately predict the output hysteresis nonlinearity of magnetostrictive actuators with radial-nested stacked configuration and further promote its application in aerospace field [37], a magnetic equivalent circuit (MEC) model that considering the parallel distribution characteristics of magnetic flux in the radial-nested magnetostrictive stack was established, a nonlinear multiphysics comprehensive dynamic (MCD) model which fully considers the nonlinear dynamic magnetization process and the MDOF mechanical dynamic system those brought by the radial-nested stacked configuration was proposed. Research on the correlation between the actuator components and the magnetic flux density was carried out as a guide for magnetic circuit design. Then a magnetic field finite element model was built, and a prototype of radial-nested stacked Terfenol-D actuator (RSTA) was fabricated, to verify the accuracy of the proposed MEC model and MCD model, respectively. Terfenol-D [38] is one of the magnetostrictive materials which has the largest magnetostrictive strain rate. The parameters in the model those cannot be obtained by measurement and calculation are identified through finite element simulation and experiments. The finite element simulation results show that the maximum error of the magnetic flux density calculated by the proposed MEC model is only 0.2%. The results of experiments demonstrate that the established MCD model can accurately describe the output characteristics of RSTA at all operating condition, and the maximum root-mean-square error is less than 1.76%. The stroke of the RSTA can reach 110 μm under an axial dimension of 70.2 mm. What's more, the bandwidth of the RSTA can still exceed 500 Hz.

The remainder of this paper is structured as follows: The establishment of the MEC model and the magnetic conduction analysis of radial-nested stacked configuration are shown in Sect. 2. In Sect. 3, the MCD model was proposed. Including an electrical input dynamics model, a nonlinear dynamic Jiles-Atherton magnetization model with the nonuniformity distribution of magnetic field and a mechanical multi-degree-of-freedom (MDOF) dynamic model considering internal load were established. The experiments on a fabricated prototype and the accuracy verification for the proposed MCD model are carried out in Sect. 4. Section 5 gives the conclusions.

2 Magnetic equivalent circuit modeling and analysis

2.1 The magnetic circuit structure

The magnetostrictive actuator with radial-nested stacked configuration as shown in Fig. 2a is mainly composed of three parts: radial-nested stack (magnetostrictive rod 1, magnetostrictive rod 2, magnetostrictive rod 3, sleeve 1 and sleeve 2), preload applying mechanism (disc spring, output rod, pre-tightening end cover and shell) and electromagnetic excitation device (coil and coil bobbin). The base, output rod and shell are all made of DT4C with extremely high magnetic permeability. But the sleeve material and end cover material are stainless steel (SUS304) with relative permeability of 1.3. To analyze the distribution of magnetic

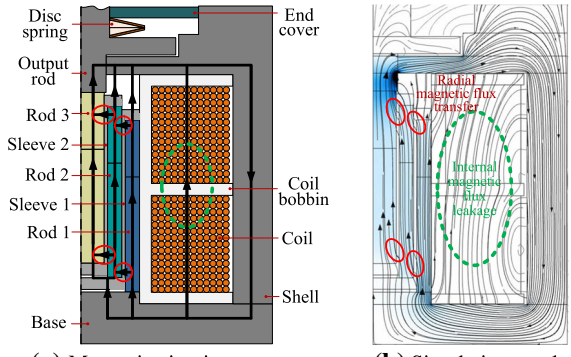

(a) Magnetic circuit structure **(b)** Simulation result

Fig. 2 Magnetic conduction analysis for a magnetostrictive actuator with radial-nested stacked configuration

field lines, a two-dimensional axisymmetric magnetic field analysis finite element model (FEM) was built in COMSOL. The simulation results are shown in Fig. 2b, which indicate that a closed magnetic circuit will be produced inside the actuator in the working process. There was obvious internal magnetic flux leakage, and the radial flux transfer between three magnetostrictive rods also exists. As shown in Fig. 2b, the magnetic field lines in the green circle are the internal magnetic flux leakage and the magnetic field lines in the red circle are the radial magnetic flux transfer between the magnetostrictive rods. The magnetic field lines split into three parts in the radial-nested magnetostrictive stack and passed through the three magnetostrictive rods, respectively.

2.2 Magnetic equivalent circuit modeling

Based on the above finite element simulation results and magnetic conduction analysis results of the magnetostrictive actuator with radial-nested stacked configuration, a MEC model is established, as shown in Fig. 3.

According to Kirchhoff's law, the magnetic flux of 15 branches in the MEC model can be solved by the following 15 equations:

$$\begin{cases} \phi_7+\phi_{10}-\phi_4=0 \\ \phi_1+\phi_5+\phi_6-\phi_{10}=0 \\ \phi_2+\phi_8+\phi_9-\phi_5-\phi_6=0 \\ \phi_3-\phi_8-\phi_9=0 \\ \phi_{11}+\phi_{15}-\phi_1=0 \\ \phi_{12}+\phi_{14}-\phi_2-\phi_{11}=0 \\ \phi_{13}-\phi_3-\phi_{12}=0 \\ \phi_4 R_{\text{shell}}+\phi_7 R_{\text{L}}-NI=0 \\ \phi_{10}R_{\text{base}}+\phi_1 R_{\text{rod1}}+\phi_{15}(R_{\text{s12}}+R_{\text{AG3}})-\phi_7 R_L=0 \\ \phi_5 R_1+\phi_2 R_{\text{rod2}}-\phi_1 R_{\text{rod1}}-\phi_{11}R_3=0 \\ \phi_3 R_{\text{rod3}}+\phi_9 R_2-\phi_2 R_{\text{rod2}}-\phi_{12}R_4=0 \\ \phi_{11}R_3+\phi_{14}(R_{\text{s22}}+R_{\text{AG4}})-\phi_{15}(R_{\text{s12}}+R_{\text{AG3}})=0 \\ \phi_{12}R_4+\phi_{13}R_{\text{or}}-\phi_{14}(R_{\text{s22}}+R_{\text{AG4}})=0 \\ \phi_8(R_{\text{s21}}+R_{\text{AG2}})-\phi_9 R_2=0 \\ \phi_6(R_{\text{s11}}+R_{\text{AG1}})-\phi_5 R_1=0 \end{cases} \tag{1}$$

where ϕ_1, ϕ_2 and ϕ_3 are the magnetic flux of magnetostrictive rod 1, rod 2 and rod 3, respectively; ϕ_4 to ϕ_{15} are the magnetic flux of other branches in the MEC model.

There are a total of 9 magnetic resistances (R_{rod1}, R_{rod2}, R_{rod3}, R_{s11}, R_{s12}, R_{s21}, R_{s22}, R_{AG1} and R_{AG2}) in the MEC model which can be calculated numerically through Eqs. (2) and (3):

$$R_{\text{axial}}=\int \frac{l_{\text{a}}}{\mu A} \tag{2}$$

$$R_{\text{radial}}=\int_{r_{\text{i}}}^{r_{\text{o}}} \frac{\mathrm{d}r}{2\pi hr\mu}=\frac{1}{2\pi h\mu}\ln\left(\frac{r_2}{r_1}\right) \tag{3}$$

where R_{axial} and R_{radial} are the axial magnetic reluctance and radial magnetic reluctance, respectively; l_{a}, A and μ are the length, cross-sectional area and permeability, respectively; r_{i}, r_{o} and h are the inner radius, outer radius and thickness of a component, respectively.

For the remaining components and air gaps with complex shapes, their reluctance can be obtained through identification or finite element simulation.

All parameters of the proposed MEC model are shown in Table 1, in which R_{L}, R_{AG3}, R_{AG4}, R_1, R_2, R_3 and R_4 are obtained through the identification of the finite element simulation results. The MEC model calculation results are converted into magnetic flux density for comparison with the finite element model (FEM) simulation results to verify its accuracy as shown in Fig. 4. Compared with the FEM calculation results, the maximum calculation error of the MEC model is less than 0.2% under different excitation currents.

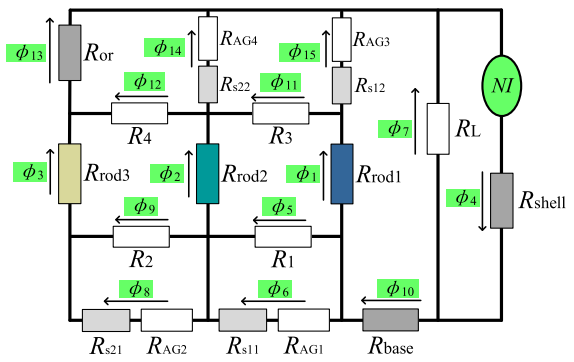

Fig. 3 The proposed MEC model, in which R_{shell}, R_{or}, R_{base}, R_{rod1}, R_{rod2} and R_{rod3} are the reluctance of shell, output rod, base, magnetostrictive rod 1, rod 2 and rod 3, respectively; R_{s11}, R_{s12}, R_{s21} and R_{s22} are the reluctance at the bottom of sleeve 1, the top of sleeve 1, the bottom of sleeve 2 and the top of sleeve 2, respectively; R_{L} is the leakage reluctance; R_1, R_2, R_3 and R_4 are the radial flux transfer reluctance; R_{AG1}, R_{AG2}, R_{AG3} and R_{AG4} are the reluctance of air gaps

Table 1 The parameters of the MEC model

Symbol	Value (H^{-1})	Symbol	Value (H^{-1})
R_{shell}	2.82×10^5	R_{s22}	6.78×10^6
R_{base}	2.37×10^5	R_{s22M}	737
R_{or}	5.02×10^5	R_L	1.37×10^8
R_{rod1}	3.47×10^7	R_1	3.78×10^6
R_{rod2}	5.29×10^7	R_2	2.53×10^7
R_{rod3}	9.50×10^7	R_3	6.99×10^6
R_{s11}	7.95×10^6	R_4	1.52×10^7
R_{s11M}	865	R_{AG1}	2.25×10^6
R_{s12}	4.45×10^6	R_{AG2}	6.25×10^6
R_{s12M}	485	R_{AG3}	8.89×10^6
R_{s21}	2.44×10^7	R_{AG4}	9.06×10^8
R_{s21M}	2650	–	–

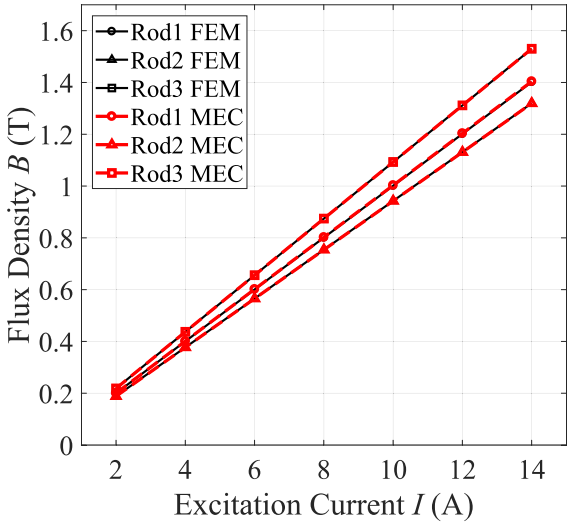

Fig. 4 Accuracy verification of the proposed MEC model

2.3 Magnetic conduction analysis

In this subsection, MATLAB & Simulink and Isight were employed to analyze the correlation between the sleeve magnetic resistance (R_{s11}, R_{s12}, R_{s21}, R_{s22}, R_1, R_2, R_3 and R_4 determined by the characteristics of the sleeves) and the magnetostrictive rods magnetic flux (ϕ_1, ϕ_2, ϕ_3 and ϕ_z). ϕ_z is the sum of the magnetic flux of three magnetostrictive rods, which determines the output performance of actuator directly.

For the correlation table in Fig. 5, "+" and "−" represent the positive or negative correlation between

	R_1	R_2	R_3	R_4	R_{s11}	R_{s12}	R_{s21}	R_{s22}	
ϕ_3	-0.01	-0.12	-0.01	-0.01	-0.88	-0.01	-0.39	+0.21	+1
ϕ_2	-0.03	+0.02	+0.01	-0.02	-0.79	-0.01	+0.06	-0.6	0
ϕ_1	0.0	-0.01	0.0	+0.01	0.0	-1.0	-0.02	-0.01	
ϕ_z	-0.02	-0.05	0.0	-0.01	-0.86	-0.41	-0.16	-0.22	-1

Fig. 5 The correlation table of magnetic resistance and output magnetic flux

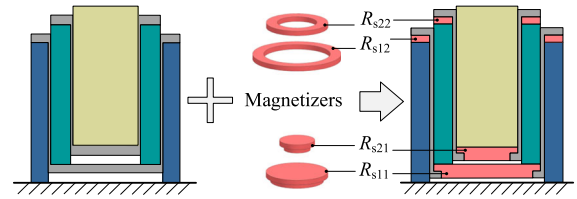

Fig. 6 The redesign of radial-nested magnetostrictive stack

the magnetic resistance and the magnetic flux, and the magnitude of the value represents the degree of influence. As shown in Fig. 5, the influence of R_1, R_2, R_3 and R_4 on the magnetic flux is very small and can be ignored. The magnetic resistance R_{s11}, R_{s12}, R_{s21} and R_{s22} have a great negative effect on the magnetic flux, which means that the smaller they are, the greater the output magnetic flux is. According to the analysis results, magnetizers are employed to change the magnetic circuit structure, as shown in Fig. 6. The magnetic resistance of R_{s11}, R_{s12}, R_{s21} and R_{s22} was reduced by adding magnetizers. The magnetizers are made of DT4C.

The increase in magnetic flux density resulting from the addition of DT4C magnetizers is shown in Fig. 7. The MEC model calculation results show that the addition of magnetizer can effectively improve the magnetic flux density on the magnetostrictive rods. The total magnetic flux density increased by 8.7%. In Table 1, R_{s11M}, R_{s12M}, R_{s21M} and R_{s22M} are the resistance of the added magnetizers.

3 Dynamic modeling

In this section, a nonlinear multiphysics comprehensive dynamic (MCD) model was proposed according to the

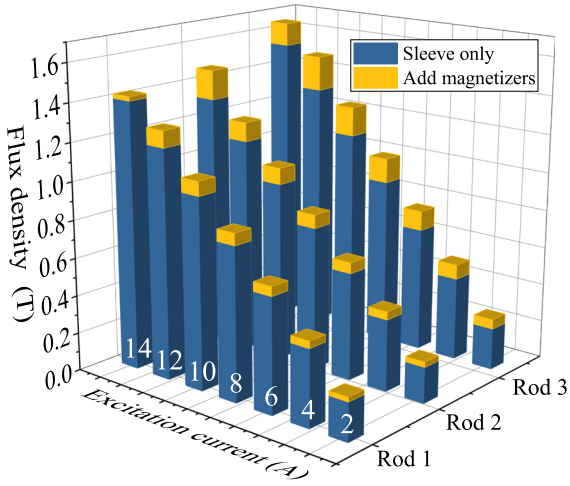

Fig. 7 Validation of the magnetic conduction optimization

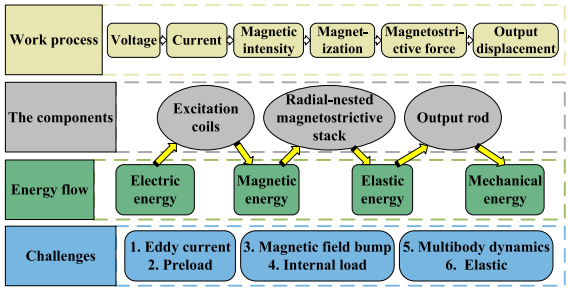

Fig. 8 The working process of the magnetostrictive actuator with radial-nested stacked configuration

working process of the magnetostrictive actuator with radial-nested stacked configuration: Firstly, the voltage input signal is amplified and transferred by the power amplifier into a current signal, which excites the coil to produce a magnetic field. Then the magnetostrictive rod is magnetized and generates magnetostrictive force under the action of the magnetic field. Finally, under the drive of magnetostrictive force, each magnetostrictive rod outputs displacement at the same time and transmits it upward through the sleeves in turn, pushing the output rod to converge into the output displacement of actuator. The whole working process is shown in Fig. 8, and there is a complex transmission of energy between physical fields.

3.1 Electrical input dynamics modeling

In the magnetostrictive actuator drive system, the power amplifier and the excitation coil are the key components to realize the electric–magnetic energy conversion. The output characteristic of the power amplifier and the inductive winding coil dynamics can be characterized as [28]:

$$G(s) = \frac{k_{\mathrm{U}}\omega_{\mathrm{U}}^2(1 + T_{\mathrm{t}}s)}{s^2 + 2\xi_{\mathrm{U}}\omega_{\mathrm{U}}s + \omega_{\mathrm{U}}^2} \tag{4}$$

where k_{U} is the amplification factor, T_{t} is the time constant, ω_{U} and ξ_{U}, respectively, represent the natural frequency and damping ratio of the system.

3.2 Nonlinear dynamic magnetization modeling

According to Eq. (1), i.e., the proposed MEC model in Sect. 2, the magnetic flux of each path in the radially nested magnetostrictive actuator can be calculated by Eq. (5).

The matrices $\boldsymbol{A}$, $\boldsymbol{B}$ and $\boldsymbol{\phi}$ are detailed in Eq. (6), in which I is the input current, N is the number of turns of the coil, and ϕ_1, ϕ_2 and ϕ_3 are the magnetic flux of magnetostrictive rod 1, rod 2 and rod 3, respectively. In Eq. (6), $R_{9,15}$, $R_{11,6}$,

$$\boldsymbol{\phi} = \boldsymbol{A}^{-1}\boldsymbol{B} \tag{5}$$

$$\boldsymbol{A} = \begin{bmatrix}
0 & 0 & 0 & -1 & 0 & 0 & 1 & 0 & 0 & 1 & 0 & 0 & 0 & 0 & 0 \\
1 & 0 & 0 & 0 & 1 & 1 & 0 & 0 & 0 & -1 & 0 & 0 & 0 & 0 & 0 \\
0 & 1 & 0 & 0 & -1 & -1 & 0 & 1 & 1 & 0 & 0 & 0 & 0 & 0 & 0 \\
0 & 0 & 1 & 0 & 0 & 0 & 0 & -1 & -1 & 0 & 0 & 0 & 0 & 0 & 0 \\
-1 & 0 & 0 & 0 & 0 & 0 & 0 & 0 & 0 & 0 & 1 & 0 & 0 & 0 & 1 \\
0 & -1 & 0 & 0 & 0 & 0 & 0 & 0 & 0 & 0 & -1 & 1 & 0 & 1 & 0 \\
0 & 0 & -1 & 0 & 0 & 0 & 0 & 0 & 0 & 0 & 0 & -1 & 1 & 0 & 0 \\
0 & 0 & 0 & R_{\text{shell}} & 0 & 0 & R_{\text{L}} & 0 & 0 & 0 & 0 & 0 & 0 & 0 & 0 \\
R_{\text{rod1}} & 0 & 0 & 0 & 0 & 0 & -R_{\text{L}} & 0 & 0 & R_{\text{base}} & 0 & 0 & 0 & 0 & R_{9,15} \\
-R_{\text{rod1}} & R_{\text{rod2}} & 0 & 0 & R_1 & 0 & 0 & 0 & 0 & 0 & -R_3 & 0 & 0 & 0 & 0 \\
0 & 0 & 0 & 0 & -R_1 & R_{11,6} & 0 & 0 & 0 & 0 & 0 & 0 & 0 & 0 & 0 \\
0 & -R_{\text{rod2}} & R_{\text{rod3}} & 0 & 0 & 0 & 0 & 0 & R_2 & 0 & 0 & -R_4 & 0 & 0 & 0 \\
0 & 0 & 0 & 0 & 0 & 0 & 0 & R_{13,8} & -R_2 & 0 & 0 & 0 & 0 & 0 & 0 \\
0 & 0 & 0 & 0 & 0 & 0 & 0 & 0 & 0 & 0 & 0 & R_4 & R_{\text{or}} & -R_{14,14} & 0 \\
0 & 0 & 0 & 0 & 0 & 0 & 0 & 0 & 0 & 0 & R_3 & 0 & 0 & R_{15,14} & -R_{15,15}
\end{bmatrix},$$

$$\boldsymbol{B} = \begin{bmatrix} 0 \\ 0 \\ 0 \\ 0 \\ 0 \\ 0 \\ 0 \\ NI \\ 0 \\ 0 \\ 0 \\ 0 \\ 0 \\ 0 \\ 0 \end{bmatrix}, \quad \boldsymbol{\phi} = \begin{bmatrix} \phi_1 \\ \phi_2 \\ \phi_3 \\ \phi_4 \\ \phi_5 \\ \phi_6 \\ \phi_7 \\ \phi_8 \\ \phi_9 \\ \phi_{10} \\ \phi_{11} \\ \phi_{12} \\ \phi_{13} \\ \phi_{14} \\ \phi_{15} \end{bmatrix} \tag{6}$$

$R_{13,8}$, $R_{14,14}$, $R_{15,14}$ and $R_{15,15}$ can be calculated as:

$$\begin{cases}
R_{9,15} = R_{\text{s12}} + R_{\text{AG3}} \\
R_{11,6} = R_{\text{s11}} + R_{\text{AG1}} \\
R_{13,8} = R_{\text{s21}} + R_{\text{AG2}} \\
R_{14,14} = R_{\text{s22}} + R_{\text{AG4}} \\
R_{15,14} = R_{\text{s22}} + R_{\text{AG4}} \\
R_{15,15} = R_{\text{s12}} + R_{\text{AG3}}
\end{cases} \tag{7}$$

When the driving frequency is low, the actuator works in quasi-static state. In this state, the magnetic field can be expressed as:

$$H_{\text{c}} = \frac{\phi}{\mu A} \tag{8}$$

where H_{c} is the magnetic intensity, ϕ is the magnetic flux, μ is the permeability, and A is the cross-sectional area.

When the frequency of the driving signal increases to a certain extent, the influence of eddy current must be considered. As shown in Fig. 9, a tubular infinitesimal element is taken from the radius r of a magnetostrictive rod, and r_1 and r_2 are the outer and inner radius of a magnetostrictive rod, respectively. r is the radius of the infinitesimal element, and d_{r} is the thickness of the infinitesimal element. For a cylindrical magnetostric-

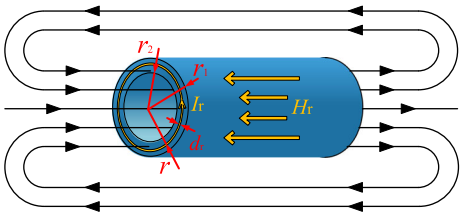

Fig. 9 The magnetic field generated by the eddy current at radius r

tive rod, $r_2 = 0$. I_r and H_r are the eddy current and the magnetic intensity generated by the infinitesimal element at radius r.

The eddy current generated by the infinitesimal element at radius r can be expressed as:

$$I_r = \frac{E}{R} = \frac{d(BS)ldr}{2\pi r dt \rho_G} = \frac{\mu_0 \mu_G l}{2\rho_G} \frac{dH_c}{dt} r dr \tag{9}$$

where μ_0 is the vacuum permeability, μ_G is the relative permeability of the magnetostrictive rod, ρ_G is the resistivity of the magnetostrictive rod, r is the radius of the infinitesimal element, E is the electromotive force, R is the resistance, B is the magnetic induction, and S is the magnetic flux area.

Then the magnetic field generated by the infinitesimal element at radius r can be expressed as:

$$H_r = \frac{NI_r}{l} = \frac{N\frac{\mu_0\mu_G l}{2\rho_G}\frac{dH_c}{dt} r dr}{l} = N\frac{\mu_0\mu_G}{2\rho_G}\frac{dH_c}{dt} r dr \tag{10}$$

where for an infinitesimal element $N = 1$.

The magnetic field generated by the entire magnetostrictive rod due to the eddy current effect can be obtained:

$$H' = \int_{r_2}^{r_1} r dr \frac{\mu_0 \mu_G}{2\rho_G} \frac{dH_c}{dt} \tag{11}$$

where r_1 and r_2 are the outer and inner radius of a magnetostrictive rod, respectively.

Therefore, when the eddy current effect was taken into consideration, the magnetic field acting on a magnetostrictive rod is:

$$H = \frac{\phi}{\mu A} - H'. \tag{12}$$

After the Laplace transform of equation 12, the magnetic field acting on a magnetostrictive rod when considering the eddy current effect is:

$$H = \frac{\phi}{\mu A(1+\tau s)} = \frac{\phi}{\mu A(1 + \mu_0\mu_G(d_o^2 - d_i^2)s/16\rho_G)} \tag{13}$$

where τ is the eddy current time constant, $d_o = 2r_1$ and $d_i = 2r_2$.

Taking into account that other components with irregular shapes such as base, U-shaped sleeves and magnetizers, etc., whose eddy current loss is difficult to quantify, air gaps between components will cause additional magnetic flux leakage, so the magnetic field acting on the magnetostrictive rod can be expressed as:

$$H = \frac{\phi}{k_f \mu A(1 + \mu_0\mu_G(d_o^2 - d_i^2)s/16k_J\rho_G)} \tag{14}$$

where k_f and k_J are the magnetic flux leakage compensation factor and the eddy current effect compensation factor, respectively.

The correlation between k_f & k_J and the MCD model's calculation error is shown in Table 2, in which E_{RMS1} to E_{RMS4} are the calculation root-mean-square error of MCD model under different working conditions. The results indicate that the factor k_f has a great contribution on the improvement of MCD model accuracy, and the average influence degree is −0.88. The influence of k_J on the MCD model accuracy increases with the increase of driving frequency, because the eddy current effect is positively correlated with frequency.

As the most widely used magnetization model, the Jiles-Atherton model can describe the magnetization process of a magnetostrictive rod using the following five equations [29]:

$$\begin{cases} H_e = H + \alpha M \\ M_{ir} = M_{an} - k\delta\left(\frac{dM_{ir}}{dH_e}\right) \\ M = M_r + M_{ir} \\ M_{an} = M_s\left[\coth\left(\frac{H_e}{a}\right) - \frac{a}{H_e}\right] \\ M_r = c_r(M_{an} - M_{ir}) \end{cases} \tag{15}$$

Table 2 The correlation between k_f & k_J and the MCD model error

	E_{RMS1} 4 A 10 Hz	E_{RMS2} 4 A 100 Hz	E_{RMS3} 4 A 200 Hz	E_{RMS4} 14 A 10 Hz
k_f	−0.87	−0.9	−0.88	−0.87
k_J	0.0	−0.03	−0.07	−0.11

where M is the magnetization, M_s is the saturation magnetization, H_e is the effective magnetic field, M_r is the reversible value of magnetization, M_{ir} is the magnetization's irreversible value, M_{an} is an hysteretic value of magnetization, α is the magnetic domain interaction coefficient which is a constant to depict the relation between the prestress and magnetic domain, c_r is the reversible coefficient, a is the shape coefficient of the magnetization curve without hysteresis, k is the pinning coefficient (the characteristic coefficient of hysteresis), and δ is the directional coefficient.

3.3 Magnetostrictive force modeling

The magnetization of a magnetostrictive rod is actually the deflection of the internal magnetic domains under the action of an external magnetic field, resulting in magnetostrictive strain and then magnetostrictive force. The prestress and the magnetic field are two main factors that affect the output force due to their effects on the magnetization and deformation process of magnetostrictive materials.

When the preload has not reached the saturation one ($F_p \leq F_s$), the magnetostrictive strain of magnetostrictive rod can be calculated by Eq. (16); otherwise ($F_p > F_s$), the magnetostrictive strain can be calculated by Eq. (17), as follows [18,39]:

$$\lambda = \left(1 + \frac{1}{2}\tanh\frac{2F_p}{F_s}\right)\lambda_s\frac{M^2}{M_s^2} \tag{16}$$

$$\lambda = \left(1 - \frac{F_p - F_s}{F_{max}}\right)\left(1 + \frac{1}{2}\tanh\frac{2F_p}{F_s}\right)\lambda_s\frac{M^2}{M_s^2} \tag{17}$$

where λ is the magnetostrictive strain; λ_s is the saturation magnetostrictive strain; F_p is the preload of a magnetostrictive rod; F_s is the saturation preload; M is the magnetization intensity; and F_{max} is the maximum magnetostrictive force of the magnetostrictive rod, which can be calculated by the following equation [40]:

$$F_{max} = \frac{3}{2}\lambda_s E_G A_G \tag{18}$$

where E_G and A_G are the initial elastic modulus and the cross-sectional area of a magnetostrictive rod, respectively.

It can be seen from equation 16 and equation 17 that the $\triangle E$ effect is characterized by the hyperbolic tangent function [39,41,42]. The magnetostrictive force F of the magnetostrictive rods can be calculated as follows [43]:

$$F = \lambda E_G A_G \tag{19}$$

3.4 Multi-degree-of-freedom mechanical dynamic modeling

In the magnetostrictive actuator with radial-nested stacked configuration, multiple components form a multi-degree-of-freedom (MDOF) dynamic system [44], in which three magnetostrictive rods become force sources when driven by a magnetic field. Sleeves, magnetizers and output rod act as elastic elements to transfer force and displacement. The established MDOF dynamic model of the actuator is shown in Fig. 10. Because the stiffness of the disc spring is much smaller than other components in the system, no matter which magnetostrictive rod, it will output displacement toward the disc spring direction. For magnetostrictive rod 1, in addition to overcoming its own mass, stiffness and damping, it should also overcome the mass, stiffness and damping of other components in the output direction, which are the loads of rod 1 inside the actuator. The same is true for magnetostrictive rod 2 and magnetostrictive rod 3.

According to the aforementioned analysis, the dynamic equation of the system can be expressed by Eq. (20):

$$\boldsymbol{M}\ddot{\boldsymbol{X}} + \boldsymbol{C}\dot{\boldsymbol{X}} + \boldsymbol{K}\boldsymbol{X} = \boldsymbol{F} \tag{20}$$

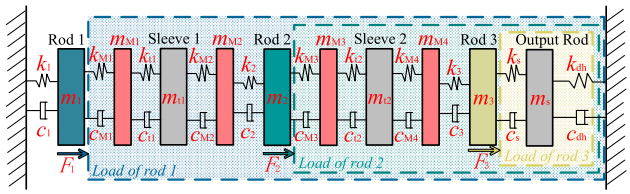

Fig. 10 Schematic of the multi-degree-of-freedom dynamic model

where $\boldsymbol{M}$, $\boldsymbol{C}$ and $\boldsymbol{K}$ are the mass matrix, the damping matrix and the stiffness matrix of the system, respectively; $\boldsymbol{X}$ and $\boldsymbol{F}$ are the displacement matrix and input matrix of the system, which can be expressed as follows:

$$\boldsymbol{M} = \begin{bmatrix} \frac{m_1}{3} + m_{\mathrm{lr1}} & 0 & 0 \\ 0 & \frac{m_2}{3} + m_{\mathrm{lr2}} & 0 \\ 0 & 0 & \frac{m_3}{3} + m_{\mathrm{lr3}} \end{bmatrix} \tag{21}$$

$$\boldsymbol{C} = \begin{bmatrix} c_1 + c_{\mathrm{lr1}} & 0 & 0 \\ 0 & c_2 + c_{\mathrm{lr2}} & 0 \\ 0 & 0 & c_3 + c_{\mathrm{lr3}} \end{bmatrix} \tag{22}$$

$$\boldsymbol{K} = \begin{bmatrix} k_1 + k_{\mathrm{lr1}} & 0 & 0 \\ 0 & k_2 + k_{\mathrm{lr2}} & 0 \\ 0 & 0 & k_3 + k_{\mathrm{lr3}} \end{bmatrix} \tag{23}$$

$$\boldsymbol{X} = \begin{bmatrix} x_1 \\ x_2 \\ x_3 \end{bmatrix}, \boldsymbol{F} = \begin{bmatrix} F_1 \\ F_2 \\ F_3 \end{bmatrix} \tag{24}$$

where m_1, m_2 and m_3 are the mass of rod 1, rod 2 and rod 3, respectively; c_1, c_2 and c_3 are the damping of rod 1, rod 2 and rod 3, respectively; k_1, k_2 and k_3 are the stiffness of rod 1, rod 2 and rod 3, respectively; x_1, x_2 and x_3 are the output displacement of rod 1, rod 2 and rod 3, respectively; F_1, F_2 and F_3 are the output force of rod 1, rod 2 and rod 3, respectively; m_{lr1}, m_{lr2} and m_{lr3} are the equivalent load mass of rod 1, rod 2 and rod 3, respectively; c_{lr1}, c_{lr2} and c_{lr3} are the equivalent load damping of rod 1, rod 2 and rod 3, respectively; k_{lr1}, k_{lr2} and k_{lr3} are the equivalent load stiffness of rod 1, rod 2 and rod 3, respectively, which can be calculated by the following equations:

$$\begin{cases} m_{\mathrm{lr1}} = m_{\mathrm{M1}} + m_{\mathrm{t1}} + m_{\mathrm{M2}} + m_2 + m_{\mathrm{M3}} \\ \qquad\quad + m_{\mathrm{t2}} + m_{\mathrm{M4}} + m_3 + m_{\mathrm{s}} \\ m_{\mathrm{lr2}} = m_{\mathrm{M3}} + m_{\mathrm{t2}} + m_{\mathrm{M4}} + m_3 + m_{\mathrm{s}} \\ m_{\mathrm{lr3}} = m_{\mathrm{s}} \end{cases} \tag{25}$$

$$\begin{cases} c_{\mathrm{lr1}} = \left(\frac{1}{c_{\mathrm{M1}}} + \frac{1}{c_{\mathrm{t1}}} + \frac{1}{c_{\mathrm{M2}}} + \frac{1}{c_2} + \frac{1}{c_{\mathrm{M3}}} \right. \\ \qquad\quad \left. + \frac{1}{c_{\mathrm{t2}}} + \frac{1}{c_{\mathrm{M4}}} + \frac{1}{c_3} + \frac{1}{c_{\mathrm{s}}} + \frac{1}{c_{\mathrm{dh}}} \right)^{-1} \\ c_{\mathrm{lr2}} = \left(\frac{1}{c_{\mathrm{M3}}} + \frac{1}{c_{\mathrm{t2}}} + \frac{1}{c_{\mathrm{M4}}} + \frac{1}{c_3} + \frac{1}{c_{\mathrm{s}}} + \frac{1}{c_{\mathrm{dh}}} \right)^{-1} \\ c_{\mathrm{lr3}} = \left(\frac{1}{c_{\mathrm{s}}} + \frac{1}{c_{\mathrm{dh}}} \right)^{-1} \end{cases} \tag{26}$$

$$\begin{cases} k_{\mathrm{lr1}} = \left(\frac{1}{k_{\mathrm{M1}}} + \frac{1}{k_{\mathrm{t1}}} + \frac{1}{k_{\mathrm{M2}}} + \frac{1}{k_2} + \frac{1}{k_{\mathrm{M3}}} \right. \\ \qquad\quad \left. + \frac{1}{k_{\mathrm{t2}}} + \frac{1}{k_{\mathrm{M4}}} + \frac{1}{k_3} + \frac{1}{k_{\mathrm{s}}} + \frac{1}{k_{\mathrm{dh}}} \right)^{-1} \\ k_{\mathrm{lr2}} = \left(\frac{1}{k_{\mathrm{M3}}} + \frac{1}{k_{\mathrm{t2}}} + \frac{1}{k_{\mathrm{M4}}} + \frac{1}{k_3} + \frac{1}{k_{\mathrm{s}}} + \frac{1}{k_{\mathrm{dh}}} \right)^{-1} \\ k_{\mathrm{lr3}} = \left(\frac{1}{k_{\mathrm{s}}} + \frac{1}{k_{\mathrm{dh}}} \right)^{-1} \end{cases} \tag{27}$$

where m_{M1}, m_{t1}, m_{M2}, m_{M3}, m_{t2}, m_{M4} and m_{s} are the mass of magnetizer 1, sleeve 1, magnetizer 2, magnetizer 3, sleeve 2, magnetizer 4 and output rod, respectively; c_{M1}, c_{t1}, c_{M2}, c_{M3}, c_{t2}, c_{M4}, c_{s} and c_{dh} are the damping of magnetizer 1, sleeve 1, magnetizer 2, magnetizer 3, sleeve 2, magnetizer 4, output rod and disc spring, respectively; k_{M1}, k_{t1}, k_{M2}, k_{M3}, k_{t2}, k_{M4}, k_{s} and k_{dh} are the stiffness of magnetizer 1, sleeve 1, magnetizer 2, magnetizer 3, sleeve 2, magnetizer 4, output rod and disc spring, respectively.

Finally, the state space model of the MDOF dynamic system can be established as follows:

$$\begin{cases} \begin{bmatrix} \dot{\boldsymbol{X}} \\ \ddot{\boldsymbol{X}} \end{bmatrix} = \begin{bmatrix} \boldsymbol{0} & \boldsymbol{1} \\ -\boldsymbol{M}^{-1}\boldsymbol{K} & -\boldsymbol{M}^{-1}\boldsymbol{C} \end{bmatrix} \begin{bmatrix} \boldsymbol{X} \\ \dot{\boldsymbol{X}} \end{bmatrix} + \begin{bmatrix} \boldsymbol{0} \\ \boldsymbol{M}^{-1} \end{bmatrix} \boldsymbol{F} \\ \boldsymbol{Y} = \begin{bmatrix} \boldsymbol{1} & \boldsymbol{0} \end{bmatrix} \begin{bmatrix} \boldsymbol{X} \\ \dot{\boldsymbol{X}} \end{bmatrix}. \end{cases} \tag{28}$$

4 Experimental evaluation

In this section, a prototype of radial-nested stacked Terfenol-D actuator (RSTA) was manufactured and a series of experiments were carried out to verify the accuracy of the proposed multiphysics comprehensive dynamic (MCD) model.

4.1 The prototype of radial-nested stacked Terfenol-D actuator

As shown in Fig. 11, rod 1 and rod 2 are tubular, and rod 3 is cylindrical, both of them are consisted of a short Terfenol-D rod of 10 mm and a long Terfenol-D rod of 20 mm, which is aim to reduce the mechanical hysteresis of single long magnetostrictive rod. The diameters of each Terfenol-D rods are shown in Table 3. The height of the RSTA prototype is 70.2 mm. The magnetizer material is DT4C, and the sleeve material is SUS304. In the prototype, the excitation coil is divided into upper and lower windings, which are independently driven by two power amplifiers to improve the dynamic response of the actuator.

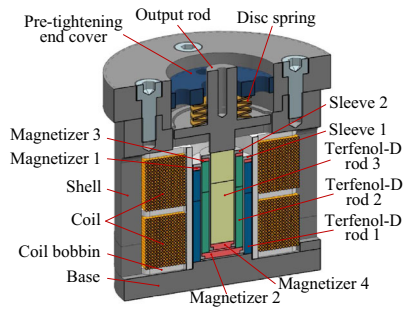

(a) The 3D digital model

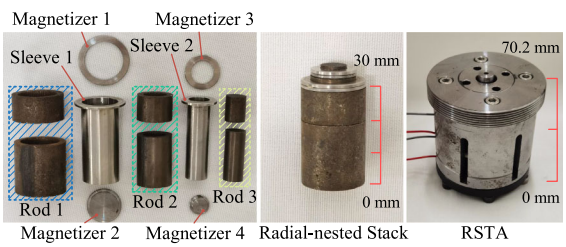

(b) The physical prototype

Fig. 11 Components of the RSTA

Table 3 The diameter of Terfenol-D rods

Name	Outer diameter (mm)	Inner diameter (mm)
Rod 1	20	15
Rod 2	14	9
Rod 3	8	–

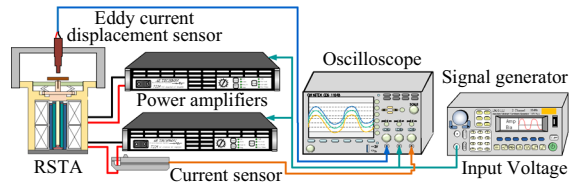

(a) Signal flow diagram

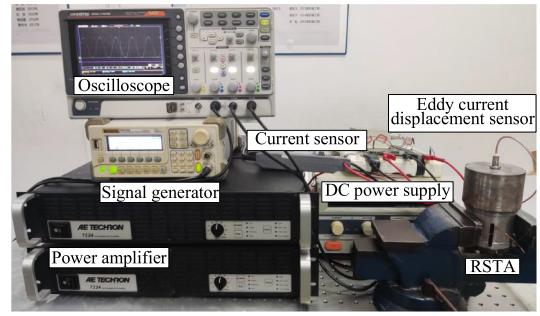

(b) Composition of test bench

Fig. 12 Experimental platform for open-loop test of the RSTA

4.2 Experimental platform

An experimental platform was built to test the open-loop performance of the RSTA, as shown in Fig. 12. The input voltage signal is generated by the signal generator (Beijing Puyuan Jingdian Technology Co., LTD, DG1022) and linearly amplified by the power amplifier (AE Techron Inc., 7224) into a current signal to directly excite the coil. Noncontact current sensor (Shenzhen Zhiyong Co., Ltd, CP800) and eddy current displacement sensor (Hangzhou Huarui Instrument Co., LTD, CZF-2) were employed to measure the output current of power amplifier and the output displacement of RSTA, respectively. The oscilloscope (Taiwan Cuswell Electronics, GDS-1104B) is responsible for collecting and storing experimental data, including the input voltage, the excitation current and the output displacement of the actuator.

4.3 Open-loop performance test

Magnetostrictive materials have inherent frequency doubling effect, and the DC bias method is adopted to eliminate it. Therefore, the input signal of the actuator used in the open-loop test is shown in Fig. 13, all of which are sinusoidal with DC bias-added signal.

For magnetostrictive materials, the application of preload can effectively increase the output stroke and

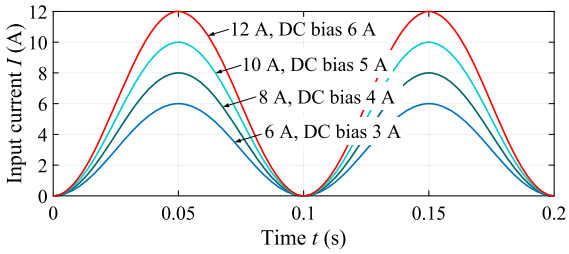

Fig. 13 The input current waveform

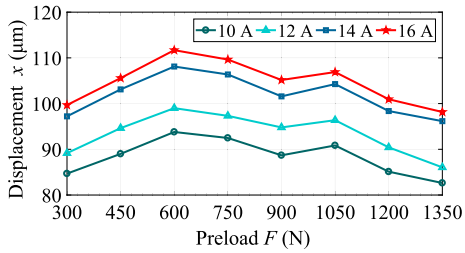

Fig. 14 The effect of preload under variable current on the RSTA output displacement

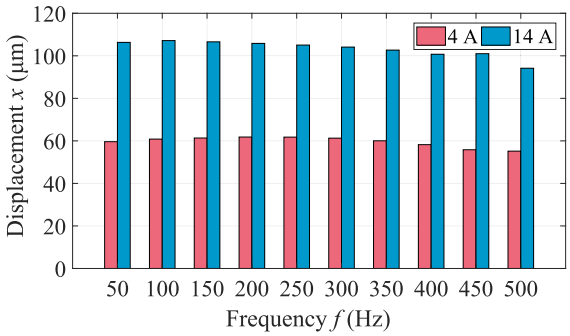

Fig. 15 The frequency response of the RSTA

improve the working reliability, because the tensile strength of Terfenol-D material is much lower than the compressive strength. The RSTA preload application device is composed of 6 disc springs in series, which reduces the stiffness while ensuring that the Terfenol-D material obtains sufficient preload. As shown in Fig. 14, a preload test was carried out, and there is an optimal preload of 600 N for the optimized RSTA. Therefore, the following experiments are carried out under a preload of 600 N. The parameters of three magnetostrictive rods for magnetostrictive force model are shown in Table 5.

Further, under the drive current of 4 A and 14 A, the influence of operating frequency on actuator output displacement amplitude is studied. The results show that under the excitation current of 4 A (14 A), the output displacement of the actuator at 500 Hz is 92.5% (88.6%) of that at 50 Hz. The obtained actuator amplitude-frequency characteristic is shown in Fig. 15, which indicate that the RSTA has a bandwidth far exceeding 500 Hz under sub-millimeter stroke.

Table 4 The parameters of multi-island genetic algorithm

Parameter	Value
Sub-Population Size	20
Number of Islands	20
Number of Generations	20
Rate of Crossover	1.0
Rate of Mutation	0.01
Rate of Migration	0.02
Interval of Migration	5

4.4 Parameter identification

The mass and stiffness of each component in the MCD model can be directly obtained by measurement, calculation or finite element simulation. However, the damping parameters ($c_1, c_{M1}, c_{t1}, c_{M2}, c_2, c_{M3}, c_{t2}, c_{M4}, c_3, c_s$ and c_{dh}) must be identified through experimental data. For the dynamic J-A model, the three magnetostrictive rods have different shapes, and a total of 12 unknown parameters (a, α, c_r and k of Terfenol-D rod 1, rod 2 and rod 3, respectively) need to be obtained through identification.

Considering the numerous components and parameters in the RSTA dynamic system, a multi-island genetic algorithm was employed to ensure the convergence of parameter identification, and its parameter settings are shown in Table 4. In order to make the dynamic model to include amplitude-related and frequency-related characteristics, the identification work was carried out at 4 A & 10 Hz, 12 A & 10 Hz, 4 A & 100 Hz and 12 A & 100 Hz, simultaneously. The objective function of the algorithm is set as a sum of the maximum error and the root-mean-square error of the MCD model calculation results compared with the experimental results, as the following equation:

$$Objective = \sum_{i=1}^{4} e_{im} + \sum_{i=1}^{4} e_{irms} \tag{29}$$

Table 5 The parameters of magnetostrictive force model

Symbol	Unit	Rod1	Rod2	Rod3
E_G	GPa	30	30	30
A_G	mm^2	137.4	90.3	50.3
F_p	N	600	600	600
F_s	N	2062	1355	754
F_{max}	N	6186	4065	2262

Table 6 The parameters of dynamic model

Symbol	Unit	Value	Symbol	Unit	Value
m_1	g	38	k_{M3}	$N \cdot \mu m^{-1}$	2077
k_1	$N \cdot \mu m^{-1}$	137	c_{M3}	$N \cdot s \cdot m^{-1}$	3486
c_1	$N \cdot s \cdot m^{-1}$	934	m_{t2}	g	4.2
m_{M1}	g	1.1	k_{t2}	$N \cdot \mu m^{-1}$	92
k_{M1}	$N \cdot \mu m^{-1}$	3161	c_{t2}	$N \cdot s \cdot m^{-1}$	6558
c_{M1}	$N \cdot s \cdot m^{-1}$	5933	m_{M4}	g	0.62
m_{t1}	g	7.1	k_{M4}	$N \cdot s \cdot m^{-1}$	506
k_{t1}	$N \cdot \mu m^{-1}$	156	c_{M4}	$N \cdot s \cdot m^{-1}$	7793
c_{t1}	$N \cdot s \cdot m^{-1}$	9906	m_3	g	13.9
m_{M2}	g	2.1	k_3	$N \cdot \mu m^{-1}$	50
k_{M2}	$N \cdot \mu m^{-1}$	939	c_3	$N \cdot s \cdot m^{-1}$	989
c_{M2}	$N \cdot s \cdot m^{-1}$	3693	m_s	g	7.1
m_2	g	25.1	k_s	$N \cdot \mu m^{-1}$	642
k_2	$N \cdot \mu m^{-1}$	90	c_s	$N \cdot s \cdot m^{-1}$	8224
c_2	$N \cdot s \cdot m^{-1}$	942	k_{dh}	$N \cdot \mu m^{-1}$	0.29
m_{M3}	g	0.72	c_{dh}	$N \cdot s \cdot m^{-1}$	934

Table 7 The parameters of Jiles-Atherton model

Symbol	Unit	Rod1	Rod2	Rod3
M_s	$kA \cdot m^{-1}$	600	600	600
a	$A \cdot m^{-1}$	3437	7365	7012
α	–	-5.5×10^{-4}	−0.0311	−0.01
c_r	–	0.401	0.4457	0.18
k	$A \cdot m^{-1}$	5904	3997	4283

where $e_{1m} \sim e_{4m}$ and $e_{1rms} \sim e_{4rms}$ are the maximum error and the root-mean-square error of the MCD model under 4 A & 10 Hz, 12 A & 10 Hz, 4 A & 100 Hz and 12 A & 100 Hz working conditions, respectively. The process of identification is to find a set of parameters that minimize the objective function.

The parameters of the dynamic model are shown in Table 6, and those of the J-A model are shown in Table 7. The stiffness parameters are calculated by Eq. (30), and the mass parameters are calculated by Eq. (31).

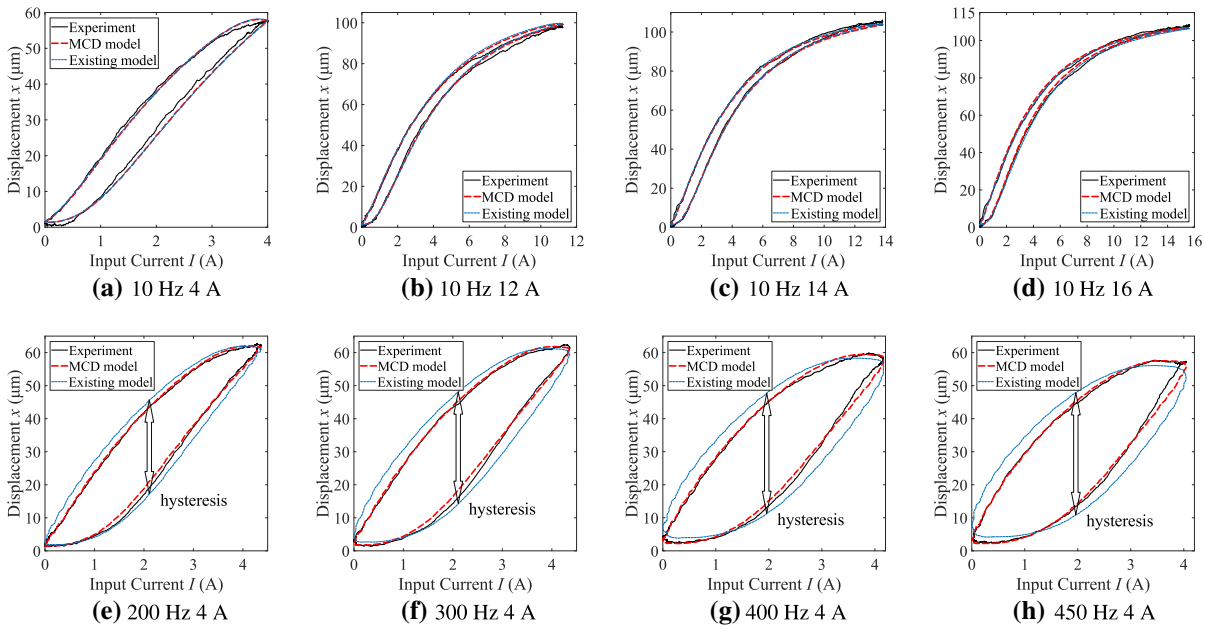

Fig. 16 Dynamic model verification in different input amplitude and frequency

$$k = \frac{EA}{l} \tag{30}$$

$$m = \rho v \tag{31}$$

where k is the stiffness, E is the elastic modulus, A is the cross-sectional area, l is the length, m is the mass, ρ is the material density, and v is the volume.

4.5 MCD model validation

The employment of the MEC model allows the MCD model to take into account the nonuniform magnetic field distribution inside the RSTA. Compared with the existing model [45] which homogenizes the magnetic field distribution in calculation by using Eq. (32), the accuracy of the proposed MCD model is not affected by the variation of RSTA operating frequency.

$$H = \frac{NI}{k_c l_c} \tag{32}$$

where N is the number of turns of the coil, I is the input current, k_c is the leakage coefficient of the magnetic flux, and l_c is the axial length of the coil.

As shown in Fig. 16, at a working frequency of 10 Hz, when the excitation current amplitude is 4A, 12A, 14 A and 16 A, both the MCD model and the existing model can accurately predict the output displacement amplitude and hysteresis characteristics of the RSTA

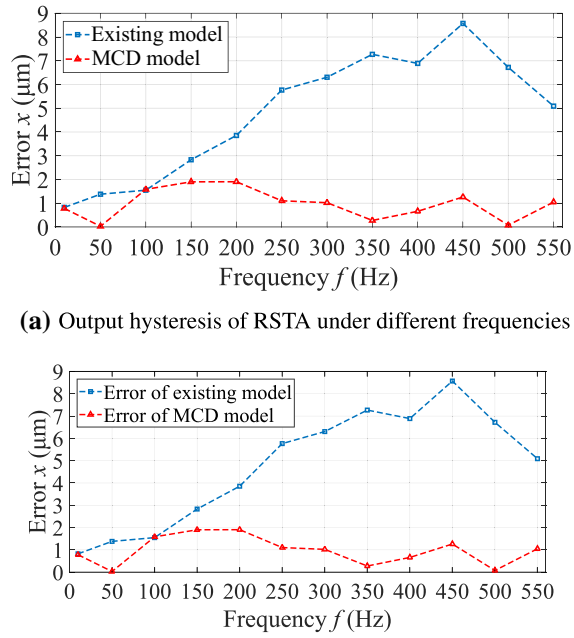

Fig. 17 Accuracy verification of the MCD model in hysteresis calculation

with a root-mean-square (RMS) error less than 1.74%. When the operating frequencies are 200 Hz, 300 Hz, 400 Hz and 450 Hz under the excitation current of 4 A, the calculation results of the MCD model are highly consistent with the experimental results, and the RMS errors are 1.1 μm (1.76%), 0.7684 μm (1.23%), 0.7122 μm (1.19%) and 0.8649 μm (1.49%), respectively. In contrast, the RMS errors of the existing model are 2.577 μm (4.12%), 3.0955 μm (4.96%), 3.6487 μm (6.1%) and 3.9357 μm (6.8%), respectively.

As shown in Fig. 17a, under a excitation current of 4 A, the experimental hysteresis and the hysteresis obtained by the MCD model simulation show the same frequency correlation. The error of the MCD model in the hysteresis calculation under different frequencies is all fluctuates around 1 μm, as shown in Fig. 17b. This is affected by the dynamic resolution (about 1 μm) of the eddy current displacement sensor (CZF-2, Hangzhou Huarui Instrument Co., LTD, measuring range:1 mm, dynamic resolution: 0.1%), so the displacement measurement has an uncertainty of 1 μm. Even the operating frequency is up to 550 Hz, the MCD model can accurately predict the hysteresis with an error only 1.0484 μm (3.1%). Under the working frequency of 0–550 Hz, the average error is only 4.16%. But for the existing model, the average error reached 17.07%. By considering the internal magnetic field distribution characteristics of RSTA into dynamic modeling, the high-frequency characteristics of the model can be effectively improved.

5 Conclusion

Magnetostrictive actuators have the characteristics of high bandwidth and high energy density, but the small output stroke and the strong hysteresis nonlinearity have become main obstacles to their further applications. Radial-nested stacked configuration enables the amplification of stroke without sacrificing bandwidth, but it also brings more serious asymmetric hysteresis nonlinearity which poses a great challenge to theoretical modeling of the actuator. In this paper, in order to describe the nonlinear dynamic characteristics of the magnetostrictive actuator with radial-nested stacked configuration and further promote its applications, a magnetic equivalent circuit (MEC) model is established to describe the magnetic characteristic of radial-nested stack; a nonlinear dynamic magnetization model is proposed with the combination of MEC model and Jiles-Atherton model; finally, by considering the multi-degree-of-freedom (MDOF) mechanical dynamic system, a multiphysics comprehensive dynamic (MCD) model was established. Based on the MEC model, the magnetoresistance sensitivity analysis of the actuator components was carried out. A magnetic field finite element model was established and a prototype of radial-nested stacked Terfenol-D actuator (RSTA) was fabricated, to verify the accuracy of the proposed MEC model and MCD model, respectively. The finite element simulation results and the experimental results indicate that:

(1) The proposed MEC model can accurately calculate the magnetic flux density distribution of the radial-nested magnetostrictive stack, the error less than 0.2%.
(2) The addition of magnetizer can effectively improve the magnetic flux density of the radial-nested stack, and the total magnetic flux density increased by 8.7%.
(3) Experimental results show that the output displacement of the RSTA reaches 110 μm and the bandwidth exceeds 500 Hz.
(4) The proposed MCD model can accurately describe the dynamic hysteresis nonlinearity of the RSTA in a wide frequency domain and a large stroke, with a RMS error less than 1.76%.

Acknowledgements This work was supported by the National Natural Science Foundation of China (Grant No. 51975275), the Primary Research & Development Plan of Jiangsu Province (Grant No. BE2021034), the National Science Foundation of Jiangsu Province of China (Grant No. BK20210294) and the Postgraduate Research & Practice Innovation Program of Jiangsu Province, China (Grant No. KYCX21_0195). (Corresponding authors: Yuchuan Zhu and Jie Ling).

Author contributions All authors contributed to the study conception and design. Material preparation, data collection and analysis were performed by [Long Chen]. The first draft of the manuscript was written by [Long Chen], and all authors commented on previous versions of the manuscript. All authors read and approved the final manuscript.

Funding This work was supported by the National Natural Science Foundation of China (Grant No. 51975275), the Primary Research & Development Plan of Jiangsu Province (Grant No. BE2021034), the National Science Foundation of Jiangsu Province of China (Grant No. BK20210294), the Postgraduate Research & Practice Innovation Program of Jiangsu Province (Grant No. KYCX21_0195).

Availability of data and materials The datasets generated during and/or analyzed during the current study are available from the corresponding author on reasonable request.

Declarations

Conflict of interest The authors declare that they have no conflict of interests.

References

1. Huang, W., Wu, X., Guo, P.: Variable coefficient magnetic energy losses calculation model for giant magnetostrictive materials. IEEE Trans. Magn. **57**(2), 1 (2021). https://doi.org/10.1109/TMAG.2020.3013393
2. Li, R., Zhu, Y., Wang, R., Li, Y., Niyomwungeri, B.: Design and analysis of a nested structure micro-displacement amplification mechanism for a galfenol-based actuator. Smart Mater. Struct. **28**(9), 095026 (2019). https://doi.org/10.1088/1361-665X/ab35c5
3. Park, Y.W., Noh, M.D.: 1-D and 2-D magnetostrictive actuators. IEEE Trans. Magn. **55**(7), 1 (2019). https://doi.org/10.1109/TMAG.2019.2891818
4. Karunanidhi, S., Singaperumal, M.: Design, analysis and simulation of magnetostrictive actuator and its application to high dynamic servo valve. Sens. Actuators, A **157**(2), 185 (2010). https://doi.org/10.1016/j.sna.2009.11.014
5. Wang, Z., Witthauer, A., Zou, Q., Kim, G.Y., Faidley, L.: Control of a magnetostrictive-actuator-based micromachining system for optimal high-speed microforming process. IEEE/ASME Trans. Mechatron. **20**(3), 1046 (2015). https://doi.org/10.1109/TMECH.2014.2363787
6. Wang, R., Zhu, Y., Jiang, Y., Chen, L.: Research on position control of bidirectional dual magnetostrictive rods-based electro-hydrostatic actuator with active rotary valve. Smart Mater. Struct. **29**(3), 035003 (2020). https://doi.org/10.1088/1361-665x/ab6485
7. Zhang, X., Li, B., Li, Z., Yang, C., Chen, X., Su, C.Y.: Adaptive neural digital control of hysteretic systems with implicit inverse compensator and its application on magnetostrictive actuator. IEEE Trans. Neural Netw. Learn. Syst (2020). https://doi.org/10.1109/TNNLS.2020.3028500
8. Tongxun Yi, M.C., Gutmark, E.J.: Dynamics and control of a high frequency fuel valve and its application to active combustion control. https://doi.org/10.2514/6.2004-4034. Paper presented at the 40th AIAA/ASME/SAE/ASEE joint propulsion conference and exhibit, Fort Lauderdale, Florida, USA, (2004)
9. Meng, A., Yang, J., Li, M., Jiang, S.: Research on hysteresis compensation control of GMM. Nonlinear Dyn. **83**(1), 161 (2016). https://doi.org/10.1007/s11071-015-2316-6
10. Gao, X., Liu, Y.: Research of giant magnetostrictive actuator's nonlinear dynamic behaviours. Nonlinear Dyn. **92**(3), 793 (2018). https://doi.org/10.1007/s11071-018-4061-0
11. Yi, S., Yang, B., Meng, G.: Ill-conditioned dynamic hysteresis compensation for a low-frequency magnetostrictive vibration shaker. Nonlinear Dyn. **96**(1), 535 (2019). https://doi.org/10.1007/s11071-019-04804-1
12. Chen, J.L., Zhang, C.L., Xu, M.L., Zi, Y.Y., Zhang, X.N.: Rhombic micro-displacement amplifier for piezoelectric actuator and its linear and hybrid model. Mech. Syst. Signal Process. **50–51**, 580 (2015). https://doi.org/10.1016/j.ymssp.2014.05.047
13. Choi, K.B., Lee, J., Kim, G., Lim, H., Kwon, S., Lee, S.C.: Design and analysis of a flexure-based parallel XY stage driven by differential piezo forces. Int. J. Precis. Eng. Manuf. **21**(8), 1547 (2020). https://doi.org/10.1007/s12541-020-00358-0
14. Chen, L., Zhu, Y., Ling, J., Feng, Z.: Development and test of a two-dimensional stacked terfenol-D actuator with high bandwidth and large stroke. IEEE/ASME Trans. Mechatron. **26**(4), 1951 (2021). https://doi.org/10.1109/TMECH.2021.3080395
15. Lee, T., Chopra, I.: Design of piezostack-driven trailing-edge flap actuator for helicopter rotors. Smart Mater. Struct. **10**(1), 15 (2001). https://doi.org/10.1088/0964-1726/10/1/302
16. Chakrabarti, S., Dapino, M.J.: Hydraulically amplified terfenol-D actuator for adaptive powertrain mounts. J. Vib. Acoust. **133**(6), 061015 (2011). https://doi.org/10.1115/1.4004669
17. Ling, M., Cao, J., Jiang, Z., Lin, J.: Theoretical modeling of attenuated displacement amplification for multistage compliant mechanism and its application. Sens. Actuators, A **249**, 15 (2016). https://doi.org/10.1016/j.sna.2016.08.011
18. Zhu, Y.C., Yang, X.L., Wereley, N.M.: Research on hysteresis loop considering the prestress effect and electrical input dynamics for a giant magnetostrictive actuator. Smart Mater. Struct. (2016). https://doi.org/10.1088/0964-1726/25/8/085030
19. Li, Y.S., Zhu, Y.C., Wu, H.T., Tang, D.B.: Modeling and inverse compensation for giant magnetostrictive transducer applied in smart material electrohydrostatic actuator. J. Intell. Mater. Syst. Struct. **25**(3), 378 (2013). https://doi.org/10.1177/1045389X13498311
20. Sun, X., Liu, Y., Hu, W., Sun, T., Hu, J.: Design optimization of a giant magnetostrictive driving system for large stroke application considering vibration suppression in working process. Mech. Syst. Signal Process. **138**, 106560 (2020). https://doi.org/10.1016/j.ymssp.2019.106560
21. Yang, Y., Yang, B., Niu, M.: Adaptive trajectory tracking of magnetostrictive actuator based on preliminary hysteresis compensation and further adaptive filter controller. Nonlinear Dyn. **92**(3), 1109 (2018). https://doi.org/10.1007/s11071-018-4112-6
22. Yang, C., Peng, Z., Tai, J., Zhu, L., Telezing, B.J.K., Ombolo, P.D.: Torque characteristics analysis of slotted-type eddy-current couplings using a new magnetic equivalent circuit model. IEEE Trans. Magn. **56**(9), 1 (2020). https://doi.org/10.1109/TMAG.2020.3009479
23. Yeo, H.K., Lim, D.K., Jung, H.K.: Magnetic equivalent circuit model considering the overhang structure of an interior permanent-magnet machine. IEEE Trans. Magn. **55**(6), 1 (2019). https://doi.org/10.1109/TMAG.2019.2897024
24. Sun, W., Li, Q., Sun, L., Zhu, L., Li, L.: Electromagnetic analysis on novel rotor-segmented axial-field SRM based on dynamic magnetic equivalent circuit. IEEE Trans. Magn. **55**(6), 1 (2019). https://doi.org/10.1109/TMAG.2019.2901002

25. Krämer, C., Kugi, A., Kemmetmüller, W.: Modeling of a permanent magnet linear synchronous motor using magnetic equivalent circuits. Mechatronics **76**, 102558 (2021). https://doi.org/10.1016/j.mechatronics.2021.102558
26. Noh, M., Park, Y.W.: Topology selection and design optimization for magnetostrictive inertial actuators. J. Appl. Phys. **111**(3), 342 (2012). https://doi.org/10.1063/1.3673431
27. Zhang, H., Zhang, T., Jiang, C.: Design of a uniform bias magnetic field for giant magnetostrictive actuators applying triple-ring magnets. Smart Mater. Struct. **22**(11), 5009 (2013). https://doi.org/10.1088/0964-1726/22/11/115009
28. Zhu, Y., Yang, X., Wereley, N.M.: Research on hysteresis loop considering the prestress effect and electrical input dynamics for a giant magnetostrictive actuator. Smart Mater. Struct. **25**(8), 085030 (2016). https://doi.org/10.1088/0964-1726/25/8/085030
29. Jiles, D., Atherton, D.: Theory of ferromagnetic hysteresis. J. Magn. Magn. Mater. **61**(1), 48 (1986). https://doi.org/10.1016/0304-8853(86)90066-1
30. Niu, M., Yang, B., Yang, Y., Meng, G.: Modeling and optimization of magnetostrictive actuator amplified by compliant mechanism. Smart Mater. Struct. **26**(9), 095029 (2017). https://doi.org/10.1088/1361-665x/aa7a83
31. Zhu, Y., Yang, X., Wereley, N.M.: Theoretical and experimental investigations of a magnetostrictive electrohydrostatic actuator. Smart Mater. Struct. (2018). https://doi.org/10.1088/1361-665x/aad071
32. Liu, Y., Gao, X., Li, Y.: Giant magnetostrictive actuator nonlinear dynamic Jiles-Atherton model. Sens. Actuators A **250**, 7 (2016). https://doi.org/10.1016/j.sna.2016.09.009
33. Ling, M., Zhang, X.: Coupled dynamic modeling of piezo-actuated compliant mechanisms subjected to external loads. Mech. Mach. Theory **160**, 104283 (2021). https://doi.org/10.1016/j.mechmachtheory.2021.104283
34. Shao, Y., Xu, M., Shao, S., Song, S.: Effective dynamical model for piezoelectric stick-slip actuators in bi-directional motion. Mech. Syst. Signal Process. **145**, 106964 (2020). https://doi.org/10.1016/j.ymssp.2020.106964
35. Gu, G.Y., Li, Z., Zhu, L.M., Su, C.Y.: A comprehensive dynamic modeling approach for giant magnetostrictive material actuators. Smart Mater. Struct. **22**(12), 125005 (2013). https://doi.org/10.1088/0964-1726/22/12/125005
36. Li, Z., Zhang, X., Gu, G.Y., Chen, X., Su, C.Y.: A comprehensive dynamic model for magnetostrictive actuators considering different input frequencies with mechanical loads. IEEE Trans. Industr. Inf. **12**(3), 980 (2016). https://doi.org/10.1109/TII.2016.2543027
37. Delaat, J.C., Breisacher, K.J., Saus, J.R., Paxson, D.E.: Active combustion control for aircraft gas turbine engines. https://doi.org/10.2514/6.2000-3500. 36th AIAA/ASME/SAE/ASEE Joint Propulsion Conference and Exhibit, Las Vegas, NV, USA, August, (2000)
38. Panduranga, M.K., Xiao, Z., Schneider, J.D., Lee, T., Klewe, C., Chopdekar, R., Shafer, P., N'Diaye, A.T., Arenholz, E., Candler, R.N., Carman, G.P.: Single magnetic domain Terfenol-D microstructures with passivating oxide layer. J. Magn. Magn. Mater. **528**, 167798 (2021). https://doi.org/10.1016/j.jmmm.2021.167798
39. Sun, L., Zheng, X.: Numerical simulation on coupling behavior of Terfenol-D rods. Int. J. Solids Struct. **43**(6), 1613 (2006). https://doi.org/10.1016/j.ijsolstr.2005.06.085
40. Chopra, I., Sirohi, J.: Smart Structures Theory, vol. 35. Cambridge University Press, Cambridge (2013). https://doi.org/10.2514/1.J053653
41. Wang, X., Wu, H., Yang, B.: Micro-vibration suppressing using electromagnetic absorber and magnetostrictive isolator combined platform. Mech. Syst. Signal Process. **139**, 106606 (2020). https://doi.org/10.1016/j.ymssp.2019.106606
42. Sun, X., Yang, B., Hu, W., Bai, Z.: Simultaneous precision positioning and vibration control for on-orbit optical payloads: an integrated actuator development and analysis. J. Vib. Eng. Technol. **9**(4), 507 (2021). https://doi.org/10.1007/s42417-020-00244-z
43. Zhu, Y., Li, Y.: A hysteresis nonlinear model of giant magnetostrictive transducer. J. Intell. Mater. Syst. Struct. **26**(16), 2242 (2015). https://doi.org/10.1177/1045389X14551434
44. Huang, M.: Multi-degree of freedom vibration theory and engineering application. Adv. Mater. Res. **250–253**, 2473 (2011). https://doi.org/10.4028/www.scientific.net/AMR.250-253.2473
45. Scheidler, J.J., Asnani, V.M.: Validated linear dynamic model of electrically-shunted magnetostrictive transducers with application to structural vibration control. Smart Mater. Struct. **26**(3), 035057 (2017). https://doi.org/10.1088/1361-665X/aa5c48